Modeling of the cross-beam energy transfer with realistic inertial-confinement-fusion beams in a large-scale hydrocode

A. Colaïtis,* G. Duchateau, X. Ribeyre, and V. Tikhonchuk
Centre Lasers Intenses et Applications, UMR No. 5107 associée au Université de Bordeaux, CNRS, and CEA, 351 Cours de la Libération, 33400 Talence, France
(Received 26 June 2014; published 7 January 2015)

A method for modeling realistic laser beams smoothed by kinoform phase plates is presented. The ray-based paraxial complex geometrical optics (PCGO) model with Gaussian thick rays allows one to create intensity variations, or pseudospeckles, that reproduce the beam envelope, contrast, and high-intensity statistics predicted by paraxial laser propagation codes. A steady-state cross-beam energy-transfer (CBET) model is implemented in a large-scale radiative hydrocode based on the PCGO model. It is used in conjunction with the realistic beam modeling technique to study the effects of CBET between coplanar laser beams on the target implosion. The pseudospeckle pattern imposed by PCGO produces modulations in the irradiation field and the shell implosion pressure. Cross-beam energy transfer between beams at 20° and 40° significantly degrades the irradiation symmetry by amplifying low-frequency modes and reducing the laser-capsule coupling efficiency, ultimately leading to large modulations of the shell areal density and lower convergence ratios. These results highlight the role of laser-plasma interaction and its influence on the implosion dynamics.

DOI: 10.1103/PhysRevE.91.013102 PACS number(s): 52.38.Dx, 52.65.Kj, 52.35.Mw, 52.38.Bv

I. INTRODUCTION

Laser-plasma interaction (LPI) is a fundamental component of inertial confinement fusion (ICF) [1–3], which involves a large variety of temporal and spatial scales. Laser-plasma interaction is commonly studied at microscopic and mesoscopic scales, using particle-in-cell and paraxial electromagnetic codes, respectively. These models allow us to study in detail nonlinear phenomena such as stimulated Raman and Brillouin scattering, filamentation, and cross-beam energy transfer (CBET), but do not allow for simulations on the long temporal and large spatial scales relevant to a whole capsule implosion. Conversely, these effects are often omitted in large-scale radiative hydrocodes, the most commonly described LPIs being refraction and inverse bremsstrahlung power deposition. The importance of taking into account more LPI effects in large-scale codes has been highlighted by theoretical and numerical works, as well as recent experiments on the NIF and OMEGA laser facilities [4–11].

Most large-scale codes rely on ray-tracing (RT) models [12] to describe the laser-beam propagation and inverse bremsstrahlung power deposition in the plasma. Modeling nonlinear LPI requires knowledge of the laser-beam intensity in the plasma. Although this quantity is not directly described by the needlelike rays of the RT model, it is possible to estimate the intensity field in the plasma by considering the neighboring ray trajectories [7,8] or from the collisional absorption [13]. These methods for modeling nonlinear LPI based on RT models suffer from a dependence of the reconstructed intensity upon the mesh resolution and the number of rays per cell. The reliance on collisional absorption or ray refraction decreases their accuracy in low-density plasmas and can produce divergent behaviors near caustics. Furthermore, the lack of consistent diffraction modeling can lead to overestimation of focusing processes and eventually artificial filamentation [13]. Inline RT-based CBET models have been successfully developed based on intensity estimations [7,8,14], although they have proven to be difficult to implement. Modeling CBET requires knowledge of the interaction of at least two electromagnetic waves and their ponderomotive excitation of an ion-acoustic wave in an *a priori* inhomogeneous and expanding plasma. This is a complex nonlinear and nonstationary process that can be studied in detail by using paraxial electromagnetic codes, which resolve the laser wavelength scales. In hydrocodes, which consider scales larger by at least an order of magnitude, the beam wave fields and plasma waves are not readily described. Development of CBET models in this framework is challenging and should be implemented step by step, using necessary simplifying assumptions. However, even simplified CBET models require, in addition to the intensity field, additional quantities that are not readily described by RT models, such as the beams propagation directions, Doppler-shifted frequencies, and downstream updates of the intensity field after energy transfer. The ray-based paraxial complex geometrical optics (PCGO) is an alternative method for describing laser beams in plasmas that presents advantages in terms of nonlinear LPI modeling in large-scale hydrocodes when compared to the RT model [13]. The PCGO model relies on a central needlelike ray that follows the standard geometrical optics laws (as in RT models) on which the wave's electric-field amplitude is reconstructed, with the restriction of Gaussian intensity profiles [15] (see [16] for a review). The PCGO method possesses the advantage of naturally modeling diffraction processes and intensity profiles, which makes it more adapted to describing nonlinear LPI. Since PCGO is limited to Gaussian rays, it must be adapted in order to be applied to ICF problems, where beams commonly have super-Gaussian envelopes and a complicated phase structure. We present in this paper a technique for modeling realistic ICF beams using PCGO Gaussian rays. Taking advantage of the PCGO formalism, a steady-state model of CBET is developed. It is applied to the case of a direct-drive capsule implosion in the framework of the OMEGA beam configuration [17], in

*Corresponding author: arnaud.colaitis@celia.u-bordeaux1.fr

two-dimensional (2D) planar geometry, and using the phase plates. Although the PCGO-based CBET model presented here has been applied to the specific case of the OMEGA facility, its formulation is sufficiently generic that it can be applied to other beam facilities setups, as well as indirect-drive configurations or planar experiments.

Similarly to the way beams are split in numerous needlelike rays in the RT model, a non-Gaussian beam profile can be approximated by a sum of Gaussian modes in the PCGO model. This splitting method presents numerous degrees of freedom and provides an opportunity to introduce variations in the 2D intensity field produced by the overlap of the Gaussian thick rays. We present in Sec. II the principles of a realistic ICF beam modeling using PCGO. Assuming a speckle pattern shaped by a kinoform phase plate (KPP), we describe a method for splitting a super-Gaussian beam in Gaussian beamlets randomly focused in a specific region around the focal spot. The resulting intensity field created by the beamlets overlap is validated against the laser propagation code MIRO [18–20] in the case of the OMEGA beam configuration. This approach presents an improvement upon the RT method as it allows for more realistic modeling of laser intensity modulations in a consistent way. A direct application of being able to accurately describe beam propagation in a large-scale hydrocode is that of CBET modeling. The theoretical description of CBET between two Gaussian rays is straightforward in a steady-state configuration. We present in Sec. III a PCGO-based CBET model describing consistent 2×2 beamlet interactions. The resulting model is used along with the realistic beam modeling method in six simulations with and without CBET enabled, with different ablators. The laser power deposition profiles and implosion symmetry in the OMEGA beam configuration are studied. Results in Sec. IV show significant low-mode amplification through two interaction geometries and decreased convergence ratios. A summary and outlook are presented in Sec. V.

II. REALISTIC BEAM MODELING

Laser beams used in direct-drive ICF are large, i.e., of the order of the capsule diameter, of top-hat envelope profile, and contain rapidly varying intensity fluctuations (speckles). In standard RT-based approaches, the envelope of these beams is modeled by bundles of needlelike rays, arranged in a way so as to reproduce the caustic of the beam by a spread in the rays' initial **k** vectors. In the framework of the PCGO approach, each ray has a Gaussian intensity profile and its thickness must be larger than a few wavelengths and smaller than characteristic plasma inhomogeneities [13,15]. Similarly to the RT approach, a large ICF beam intensity envelope can be modeled by a sum of smaller thick rays called beamlets so as to ensure the validity of the aforementioned assumptions on the Gaussian ray thickness. Compared to the RT method, splitting a beam using thick rays leads to additional degrees of freedom: The beamlets can be focused at different locations to create perturbed intensity fields. We describe in this section a method to split realistic ICF beams in bundles of thick rays in order to reproduce global beam characteristics and overall intensity fluctuation statistics (see Fig. 1 for a general illustration of the method).

A. Virtual circle

The Rayleigh range of a Gaussian beam with a wavelength λ and a radius at the focal spot w_0 is $z_R = \pi w_0^2/\lambda$. The smaller beamlets that constitute a split beam have significantly shorter Rayleigh ranges than the main beam. Such beamlets will rapidly focus and diverge, thus limiting the applicability of PCGO-based beam splitting to relatively small regions. To that extent, a beam is subdivided in beamlets only in the near-field region, where by near field we mean close to the target plasma, i.e., close to the region considered in hydrodynamical simulations. We define a virtual circle in two dimensions and a sphere in three dimensions that encircle the plasma at all times, large enough to account for plasma expansion. A circle of radius 0.8 cm centered on the capsule is large enough to contain the plasma expansion of a standard direct drive implosion. Beamlets are initialized at the virtual circle by splitting an intensity profile computed from a given focal spot profile. At each hydrodynamical time step, the beamlets are propagated in vacuum from the virtual circle to the edge of the hydrodynamical mesh. The propagation and interaction in the plasma are then resolved as in standard hydrocode-based PCGO [13].

We consider an ICF beam modulated by a KPP. The beam is characterized at the focal spot by a width r_0 and a correlation radius $\rho_0 = \lambda_0 F/\phi$ (i.e., the mean radius of the speckles), where F is the focal length of the final focusing lens and ϕ its diameter. The super-Gaussian beam envelope intensity $I(r)$ reads

$$I(r) = I_0 \exp(-|r/r_0|^n), \tag{1}$$

with I_0 the central intensity at focal spot, r the transverse coordinate, and n the order of the Gaussian beam. The overall beam envelope intensity of a partially coherent order-n Gaussian beam can be computed at a distance z using [21]

$$I(z,r) = [I_0 e^{-|r/r_0|^n}] * \left[\pi^{-3}\left(\frac{z}{z_0}\right)^{-2} \chi_{B(0,\pi z/z_0)}\left(\frac{r}{r_0}\right)\right], \tag{2}$$

where $z = 0$ at the focal plane, $z_0 = k_0\rho_0 r_0$ (with k_0 the vacuum wave number), $\chi_{B(a,b)}(r)$ represents a Heaviside distribution centered on a and of radius b, and the asterisk is a convolution product. Equation (2) is computed numerically using a fast Fourier transform from the known distribution at the focal spot to the intensity distribution at the virtual circle.

B. Beam splitting

From the beam envelope intensity at the virtual circle I_v^{FFT}, the beam must be divided in such a way that the sum of the beamlet intensities reproduces that of the whole beam. The splitting problem is simplified by fitting an order-n super-Gaussian distribution function to I_v^{FFT}, e.g., using a nonlinear least-squares method. The resulting fitted intensity profile is characterized by a central intensity I_{0v}, thickness r_v, and order n_v, defined at the virtual circle. Although I_v^{FFT} is not exactly of super-Gaussian shape, we note little difference between the fit (about 2%) and the requested profile. Moreover, energy conservation is ensured by renormalization. The splitting of a super-Gaussian distribution into a finite sum of Gaussian

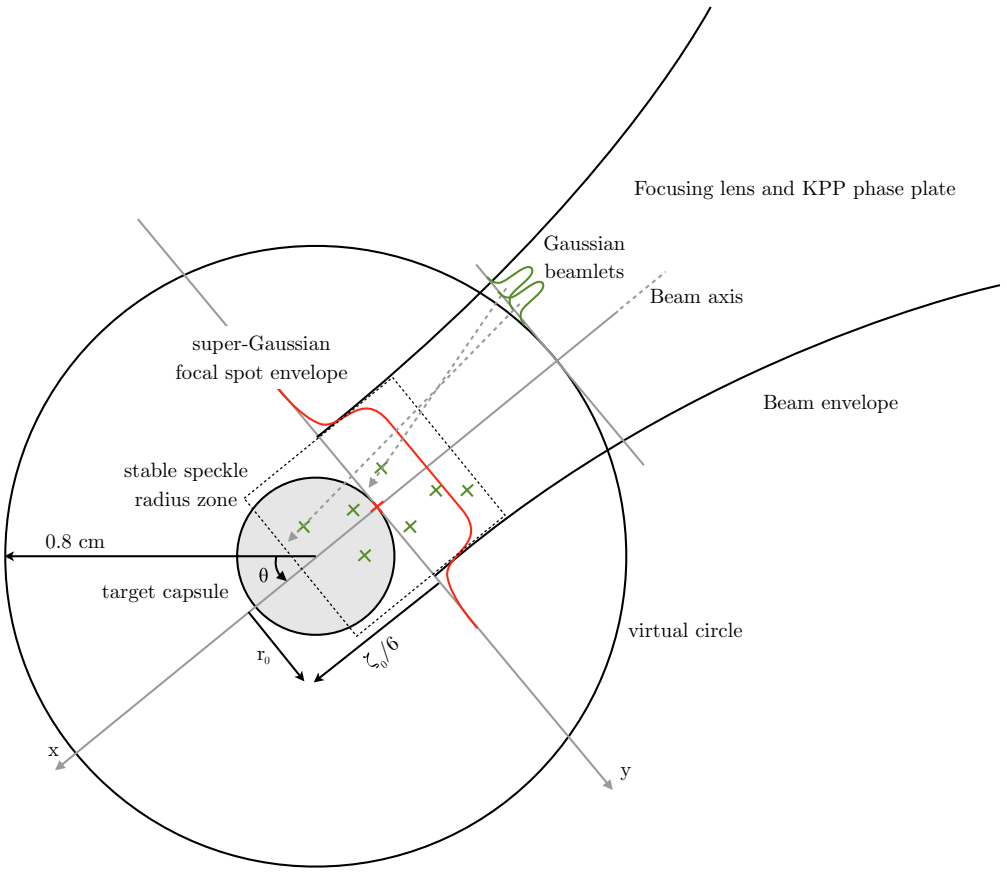

FIG. 1. (Color online) Diagram of the virtual circle defined for an ICF direct drive configuration. The capsule is represented as a gray-filled circle. Beam parameters are computed at a virtual circle (black circle) of 8 mm radius from the focal spot intensity profile represented in red (grey), the KPP, and the focusing lens parameters. The overall intensity profile at the virtual circle is combined from Gaussian beamlets, represented in green (light grey), individually focused pseudorandomly in a region around the focal spot in which the speckle radius is stable (black dotted box). Here x and y denote the local coordinate system in the direction of propagation and transverse to the beam, respectively.

distributions can be expressed as

$$I_{0v}\exp\left(-\left|\frac{r}{r_v}\right|^{n_v}\right)=\sum_{k=1}^{N}I_{0v}^{k}\exp\left[-2\left(\frac{r-\mu_v^k}{w_v^k}\right)^2\right], \quad (3)$$

where N is the number of beamlets, k is the beamlet index, and I_{0v}^k, w_v^k, and μ_v^k are the central beamlet intensity, beamlet thickness, and offset from the main beam centroid, respectively. The curvature radius and propagation vector of each beamlet were left out of this expression as these are set so as to control the beamlet focal points (see Sec. II C). For N beamlets, there are $3N$ degrees of freedom in Eq. (3). Although a nonlinear least-squares fit could provide these $3N$ parameters, this procedure is delicate, especially for large values of N. The problem is simplified by assuming that the beamlets defined at the virtual circle have the same width $\hat{w}_v$ and are equally spaced in μ_k. The values of I_{0v}^k are computed using an analytical formula described in Appendix A and by ensuring energy conservation. These values are functions of two parameters only: $\mathcal{R}=\hat{w}_v^0/\rho_0$ and N, where ρ_0 is the correlation radius of a real speckle pattern and $\hat{w}_v^0$ is the beamlet radius at its focal spot. Both parameters control the pseudospeckle pattern, as described in the next section.

C. Beamlet focusing and pseudospeckle radius

The longitudinal large-scale variation of a speckle pattern defined by a beam envelope radius r_0 and a correlation radius ρ_0 is characterized by the length scale $z_0=k_0\rho_0 r_0$ [21]. The speckle radius of such a beam is stable along the distance $\zeta_0=z_0/\pi$ from the focal plane. The transverse scale of the beam at the focal plane is determined by the radius r_0, often available from experimental data. The distances ζ_0 and r_0 define a box around the focal spot where the speckle pattern varies slowly. The N beamlets defined at the virtual circle are randomly focused in this box by setting accordingly their radii of curvature and $\mathbf{k}$ vectors. The focal spots of the beamlets are scattered by assuming a binormal distribution centered on the focal spot (x_F, y_F) of the beam. The corresponding probability density function $\mathcal{F}$ reads

$$\mathcal{F}=\frac{1}{2\pi\sigma_1\sigma_2}\exp\left(-\frac{(x-x_F)^2}{2\sigma_1^2}-\frac{(y-y_F)^2}{2\sigma_2^2}\right), \quad (4)$$

where we have chosen a diagonal covariance matrix and σ_1 and σ_2 are the standard deviations along the x and y directions, where the x coordinate is along the beam direction and the y coordinate is in the focal plane (see Fig. 1). We define σ_1 so that 99,7% of the focal points are located in the $[-\zeta_0/2,\zeta_0/2]$ interval and 68% are located in the $[-\zeta_0/6,\zeta_0/6]$ interval, i.e.,

$\sigma_1 = \zeta_0/6$. The choice of σ_2 is less sensitive as any random focal point outside the beam caustic is repicked. We define $\sigma_2 = 2r_0$. We note that because points outside the beam caustic are redrawn, the 2D distribution of focal points is not strictly binormal.

The remaining degrees of freedom N and $\mathcal{R}$ are set by comparing the vacuum intensity map produced by the beamlets to the laser propagation code MIRO [18–20] that solves the paraxial equation for the laser electric field. As a rule of thumb, N can be taken as the ratio of the radius of the whole beam at focal spot to the speckle radius. For the super-Gaussian beam of the order 4 (SG4) at the wavelength of 351 nm equipped with a KPP, $\rho_0 \simeq 2.33$ μm and $r_0 = 352$ μm, giving $N = 151$. In practice, the resolution of the hydrodynamical grid is much larger than the speckle width, which spatially smoothes the intensity field and its interaction with the hydrodynamics. Consequently, instead of reproducing the exact beam speckle pattern at the focal spot, we model large pseudospeckles, typically 3–10 times larger in radius than the real speckles. This is set through the $\mathcal{R}$ parameter, which controls the beamlet radius at the virtual circle. Because the pseudospeckles are large, the number of beamlets N can be chosen smaller, typically by a factor of 2. The parameters N and $\mathcal{R}$ indirectly control the contrast of the beam and the 2D pseudospeckle pattern. It is important to set these two parameters by comparing the generated 2D intensity field to a paraxial solution. It has been found that the pseudospeckle width remains small enough compared to the typical hydrodynamic mesh resolution employed in ICF implosions. Thus, the choice of the pseudospeckle width is not critical to the hydrodynamics response, especially when considering the effects of electron thermal conduction. The aim here is to focus on intensity statistics to model the beam energy exchange and other nonlinear LPI processes rather than to study the direct influence of the speckle distribution on the small-scale hydrodynamics through the linear inverse bremsstrahlung absorption.

D. Comparisons to MIRO

We consider a setup similar to the OMEGA facility [22], where the laser beams at a wavelength of 351 nm are equipped with the KPPs and have at the focal spot a super-Gaussian distribution (1) with $n^{\mathrm{SG4}} = 4.1$ and $r_0^{\mathrm{SG4}} = 352$ μm. The lens diameter is $\phi^{\mathrm{SG4}} = 0.27$ m and focal length is $F^{\mathrm{SG4}} = 1.80$ m. Results for the 2D intensity field as computed by MIRO using the same SG4 KPP data are shown in the top panel of Fig. 2. In order to compare MIRO to PCGO in the hydrocode CHIC in the same conditions, the results from MIRO are convolved with the hydrodynamical mesh resolution used for the simulations (see Fig. 2, middle). The bottom panel of Fig. 2 shows the 2D intensity field obtained using the splitting algorithm for $N = 100$ and $\mathcal{R} = 7$, in a simulation domain of 180×180 grid points in a box of 4×1.2 mm^2.

Although the realizations presented in Fig. 2 look differently, the splitting algorithm described here reproduces accurately the intensity statistics for normalized intensities $I/\langle I\rangle > 0.09$ (see Fig. 3, top), where $\langle I\rangle$ is the mean intensity. The statistics for lower-intensity values is less accurately reproduced, owing to the large thickness of the pseudospeckles.

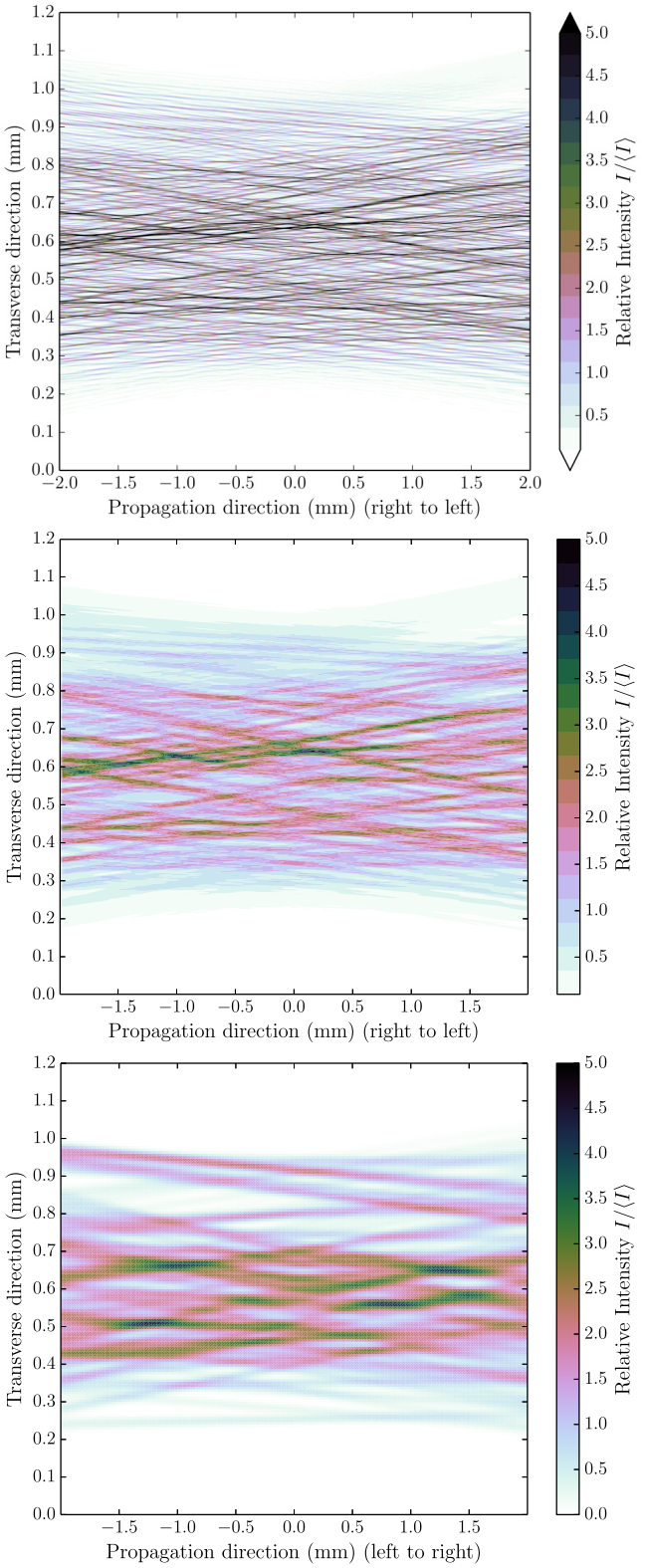

FIG. 2. (Color online) Plot of the 2D intensity field as computed by MIRO for the OMEGA beam configuration with an SG4 KPP, with (middle) and without (top) 2D convolution to the mesh resolution used for the comparison with PCGO, i.e., $dx = 22$ μm and $dy = 6.7$ μm. The bottom shows the corresponding results using the splitting algorithm and PCGO, projected onto the hydrodynamical mesh. Intensity is normalized to the average intensity of the unconvolved MIRO data $\langle I\rangle = 1.87\times10^{11}$ W/cm.

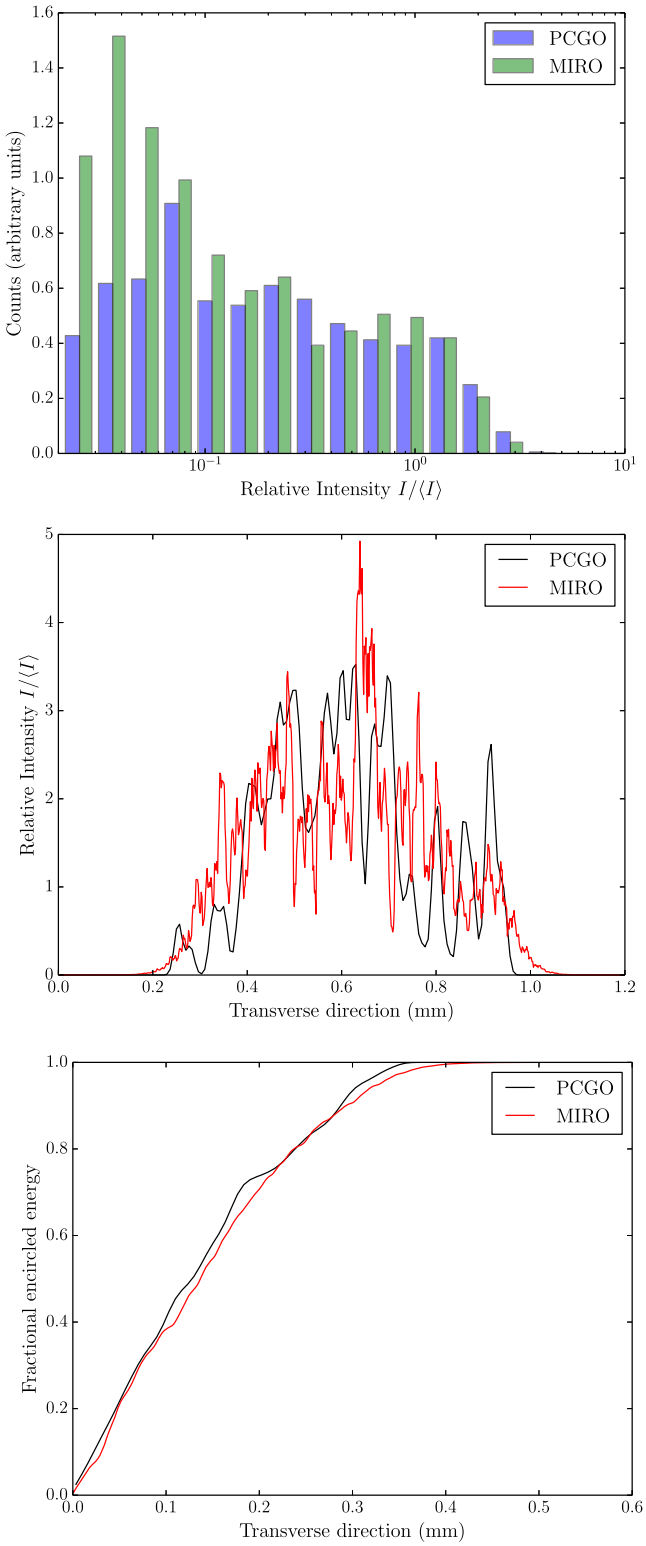

FIG. 3. (Color online) Shown on the top is a histogram of the 2D intensity field illustrated in Fig. 2 for the convolved MIRO data in green (lighter gray) and for PCGO in blue (darker gray). The middle shows an intensity profile at the focal spot from convolved MIRO data in red (gray) and PCGO in black. Intensity is normalized to the average intensity of the convolved MIRO data $\langle I\rangle = 2.00\times10^{11}$ W/cm. The bottom shows the fractional encircled energy as a function of radius, in the focal plane, for the convolved MIRO data in red (gray) and PCGO in black.

This is acceptable when studying nonlinear LPI, where it is the higher intensities that are of interest. Decreasing N at constant $\mathcal{R}$ would effectively reduce this discrepancy but would degrade the contrast away from the beam's focal spot. Similarly, decreasing $\mathcal{R}$ at constant N would also increase the low-intensity statistics. However, low values of $\mathcal{R}$ lead to shorter Rayleigh ranges for the beamlets, which limit the applicability of the splitting method. Comparing intensity slices at the focal spot shows overall agreement (see Fig. 3, middle). The fractional encircled energy of the PCGO beam is rather close to the convolved MIRO data (Fig. 3, bottom), with a slightly steeper cutoff in the wings of the beam. This difference is acceptable in the case of direct-drive configurations where there is no laser entrance hole to fit in and the wing intensity information will be lost as many beams overlap over the target in 2D or 3D configuration. Both profiles have similar contrasts, with $C_{\mathrm{PCGO}} \simeq C_{\mathrm{MIRO}} = 0.66$, where the contrast is defined as

$$C = \frac{\langle I^2\rangle - \langle I\rangle^2}{\langle I\rangle^2}. \tag{5}$$

We note that the contrast of the unconvolved MIRO data is $C = 1$, which is consistent with a pure speckle pattern.

III. CROSS-BEAM ENERGY TRANSFER

The CBET model presented here is based on the thick-ray description of laser beams using PCGO. The intensity of each thick ray is well described and can be used in the computation of nonlinear laser-plasma interactions. We consider two Gaussian beamlets crossing at an angle θ. The steady-state power transfer T between the higher-frequency beam 1 and lower-frequency beam 2 reads [23]

$$T = \frac{hI_0^1}{2\beta}\ln\{\exp(-\hat{w}_2) + \exp(\hat{w}_1)[1-\exp(-\hat{w}_2)]\}, \tag{6}$$

where $\hat{w}_1$ and $\hat{w}_2$ are normalized beam widths at the exit of the interaction region, I_0^1 is the pump beam's on-axis intensity, β is the imaginary part of the ion-acoustic response to the ponderomotive force, and h is a unit height. The downstream powers of the pump and probe beamlets P_1' and P_2' read

$$P_2' = P_2 + T, \quad P_1' = P_1 - T, \tag{7}$$

where P_1 and P_2 are the upstream powers of the pump and probe beams, respectively. Here β is the nonlinear coupling coefficient [24]

$$\beta = \frac{\omega_e^2\omega_s^2\nu_s\omega}{\omega_2\nu_2\left[\left(\omega_s^2-\omega^2\right)^2 + 4\nu_s^2\omega^2\right]}, \tag{8}$$

where ω_e is the electron plasma frequency, $\omega = \omega_1 - \omega_2$ is the difference in beam frequencies, $\omega_s = c_s|\mathbf{k_2} - \mathbf{k_1}|$ is the ion-acoustic frequency at the beat wave number with c_s the ion-acoustic velocity, ν_2 is the group velocity of the lower-frequency beam, and ν_s is the damping rate of the ion-acoustic waves. Variables related to plasma parameters are computed and interpolated at the CBET coordinates from the hydrodynamical grid. The Doppler shift of beam frequencies due to the plasma flow is taken into account in the computation of β through the frequency shift term ω.

For a Gaussian beam, it can be shown that the normalized width at the exit of the interaction region $\hat{w}_k$ reads

$$\hat{w}_k = |a_0|^2 r_{1k} \frac{\sqrt{2\pi}\beta w_0^k}{|\sin\theta|}, \tag{9}$$

where w_0^k is the beam width at the start of the interaction region, $r_{1k} = I_0^k/I_0^1$ is the intensity ratio of the beams ($r_{11} = 1$), and $a_0^2 = (v_{\rm osc}/c_s)^2(m_e/m_i)$ is the squared electromagnetic potential at the maximum of beam 1, where $v_{\rm osc}$ is the quiver velocity of the electrons and m_e/m_i is the ratio of the electron to ion mass. Equation (9) diverges for $\sin\theta = 0$. In that configuration, the two beams share one centroid, thus creating an infinite interaction region, leading to maximum gain, i.e., pump depletion. In practice, intersection of beamlet centroids at $\theta = 0^\circ$ or 180° are never observed in our simulations.

The spatial configuration of the CBET causes the two beams to have different intensity distributions after the transfer, i.e., they do not remain Gaussian [24]. In general, the output intensity profile can exhibit more than one intensity peak and be highly skewed. In order to work within the limitations of the thick-ray model, we assume the intensity distribution of a beam after an energy transfer remains Gaussian, with the same width as before the energy exchange: The amount of power transferred between beams is only impacted on their intensity. This assumption is reasonable as for these deformations to be significant in terms of influence on the small-scale hydrodynamics, a very high mesh resolution would be required. Furthermore, we neglect changes in centroids directions of the crossed beams. This phase distortion due to CBET is theoretically zero when the energy exchange is maximum (i.e., when β is maximum). Although the PCGO model is well suited to take into account this second-order effect, it is not accounted for in the present version. We make the further approximation that the energy-transfer region is pointlike, i.e., we do not project intensity variations inside the transfer region onto the hydrodynamical mesh and beam parameters are modified at the point where the centroids cross each other. Finally, because the transfer regions are modeled as being pointlike, we consider intersections between two thick rays at a time only, i.e., overlapping energy-transfer regions are treated separately and in a chronological order. Once the energy transfer between two beams has been computed and their intensities updated, their phases are recomputed from the point of crossing along the central rays by reintegrating the Riccati equations (see [13,15]). Resolving the stack of CBET intersections in a chronological and consistent order requires specific algorithms of intersection sorting, ordering, and identification of loops, which are detailed in Appendix B. Simplification of this stack can be achieved by neglecting CBET interactions for which $\beta < 5\times10^{-4}\beta_{\rm max}$. The cutoff value for β has been chosen so as to consider the maximum number of beamlet intersections as possible. Lower cutoff values do not yield different results.

The PCGO-based CBET code has been validated by conducting simulations of the interaction of two frequency-shifted Gaussian beamlets at resonance and off resonance, comparing the steady-state probe amplification for two pump intensities of 10^{15} and 10^{16} W/cm^2 and for probe to pump intensity ratios ranging from 10^{-4} to 10. Simulation results were found to be in agreement with the theoretical results presented in Ref. [25]. Further validation was conducted for the energy exchange between two Gaussian beams consisting of 100 beamlets each. The total energy exchange downstream of the intersection region (i.e., of the 10^4 intersections) was compared to the theoretical energy exchange for two beams with Gaussian envelopes. The relative error was found to be less than 1% for a wide range of $\hat{w}_k$ and probe to pump intensity ratios. The error was found to peak locally at 6% around $\hat{w}_k \sim 1$.

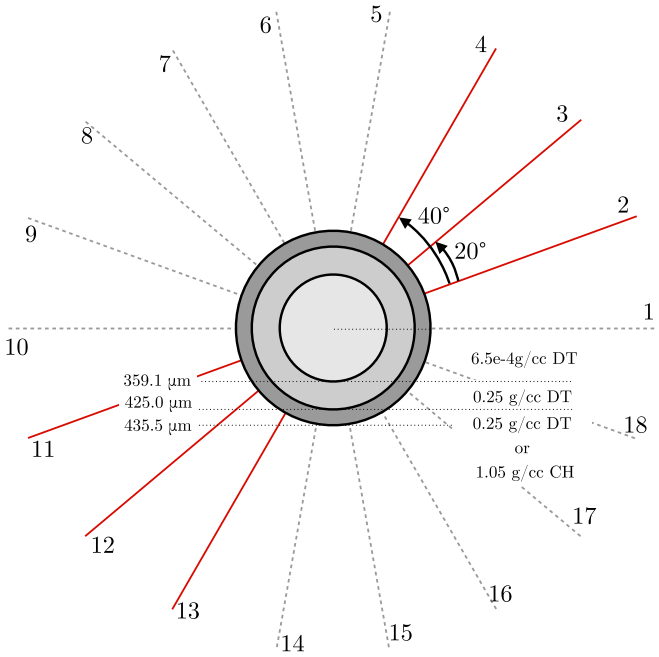

FIG. 4. (Color online) Diagram of the capsule and beam configuration: 18 beams separated by intervals of 20°, focused on the exterior surface of the ablator and following the SG4 phase plate configuration of $n^{\rm SG4} = 4.1$, $r_0^{\rm SG4} = 352$ μm, $\lambda = 0.354$ μm, $\phi^{\rm SG4} = 0.27$ m, and $F^{\rm SG4} = 1.80$ m. Beam centroids are represented as numbered lines (beamlets are not shown). Dashed gray lines represent beams that do not interact through CBET. Red (dark gray) solid lines represent beams that can interact with each other by groups of 4, as detailed in Table I.

With the power exchange being known analytically and all intersections being solved in chronological order, the energy is naturally conserved in the present CBET model. It is also worth mentioning that the beamlet-related quantities required to compute an energy transfer (i.e., width and intensity) are always well defined by PCGO, even for normally incident beamlets on the critical density and at turning points. This property that the intensity and width of PCGO beamlets do not diverge near or at the critical density (see [13,16]) is a strong motivation for its use for CBET computations and nonlinear LPI in general.

IV. APPLICATION TO DIRECT-DRIVE IMPLOSION

A. Simulation setup

The OMEGA laser facility at the Laboratory for Laser Energetics, Rochester University, can use up to eight rings of

beams arranged at constant latitudes, for a total of 60 beams. At a given longitude (or azimuth), beams are coplanar by bundles of 4, with two beams separated by angles of at least 20° or 40° and the other two beams in symmetrical positions with respect to the capsule (see Appendix C for detailed OMEGA beam angular configurations).

We consider a direct-drive capsule implosion in a 2D planar geometry. In order to reflect the 20° angular separation of the OMEGA beams in a given constant azimuth plane, the capsule is compressed using equally spaced beams separated by 20°, i.e., 18 beams (see Fig. 4). Each beam is split in beamlets with $\mathcal{R} = 10$ and $N = 60$, focused randomly so as to reproduce a pseudospeckle pattern consistent with the intensity statistics of the SG4 KPP near the focal plane, smoothed with the hydrodynamical mesh resolution. Each beam has a different set of random generator seeds, so each of them produces a different pseudospeckle pattern with a similar statistics, leading to a asymmetrical laser irradiation. Consequently, the simulation domain englobes the 360° of the cylinder, without assuming any hydrodynamical symmetries. Although it is numerically costly, this approach of a full cylinder modeling possesses the advantage of not cutting out any modes in the irradiation profile. An additional simulation without CBET is conducted, hereafter referred to as the reference case, in order to provide a baseline for the capsule compression, as the modeling of the pseudospeckles alone is expected to yield some degree of capsule deformation. The interaction conditions are shown in Table I.

TABLE I. Three simulated cases summarizing the interacting beam numbers and CBET angles of the beams centroids. Each case is conducted twice, with a deuterium-tritium (DT) and a CH ablator.

Case	Interacting beams	CBET main angles
reference case	none	none
A	2, 3, 11, 12	20°, 160°, 180°
B	2, 4, 11, 13	40°, 140°, 180°

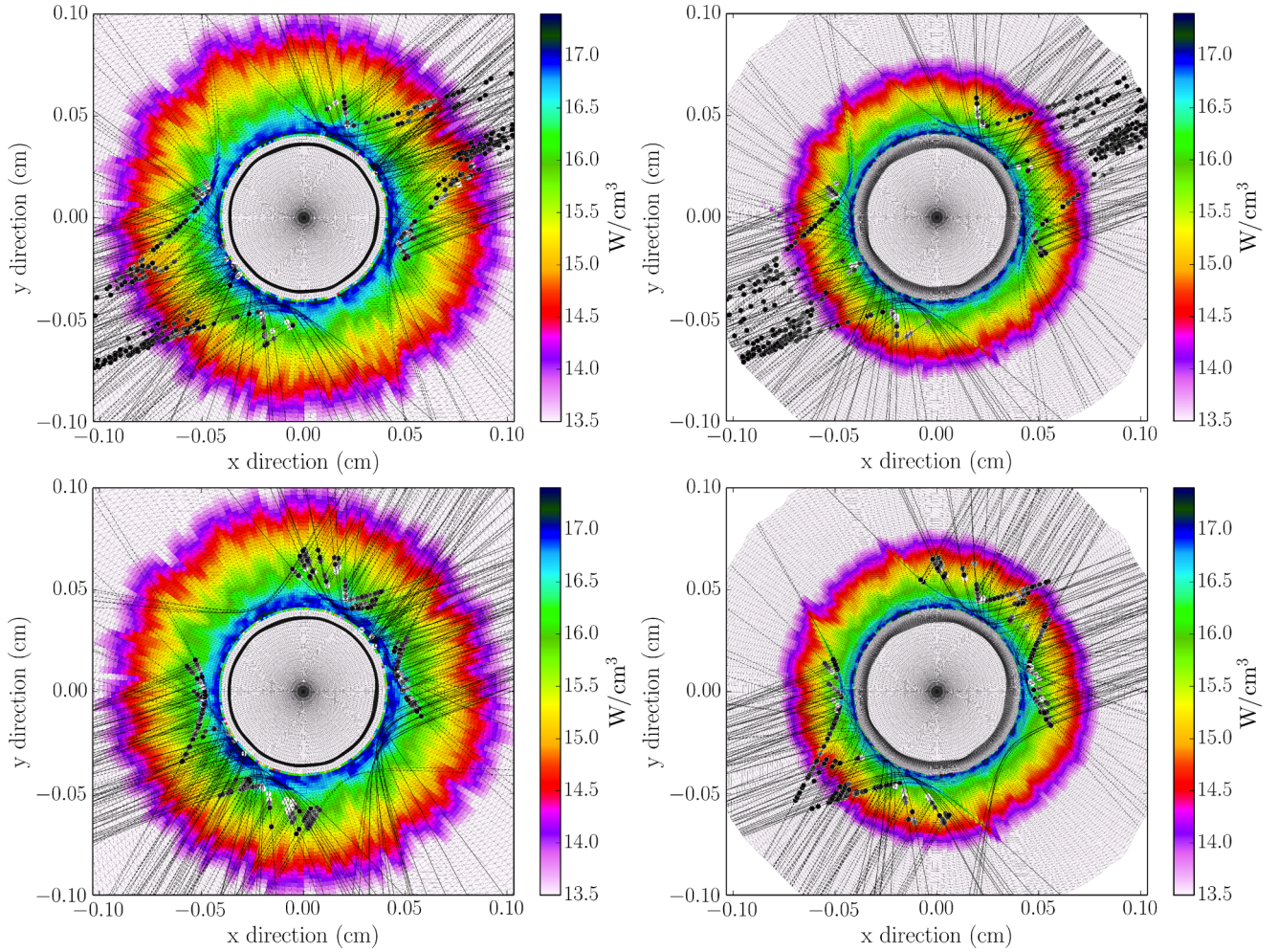

FIG. 5. (Color online) Volumic power absorbed in plasma by the inverse bremsstrahlung at about half of the laser pulse duration, i.e., after 600 ps of simulation, on a logarithmic scale. Volumic values are computed assuming a unit height of 1 cm. The top figures are from case A and the bottom figures from case B. The figures on the left present results using a CH ablator and those on the right with a DT ablator. Beamlet centroids for beams 2 and 11 are shown as solid black lines for all cases. Beamlets centroids for beams 3 and 12 for the top figures and 4 and 13 for the bottom figures are shown as dashed black lines (see Fig. 4 for beam numbering). Valid ray intersections for which CBET has been computed are indicated with gray-shaded dots, ranging from a probe gain of 1.5 in white to a probe gain of 1.01 in black.

We consider two CBET cases where the energy transfer is allowed only between four sets of beams, in order to model coplanar intersections of the real 3D OMEGA configuration (see Table I). The remaining beams that do not interact via CBET provide the global irradiation symmetry needed to implode the target. For simplicity, beamlets from the same beams are not allowed to interact with each other: Their intersection angle is narrow enough that the probe gains are small. Cross-beam energy-transfer computations are enabled after 100 ps of simulation so that a coronal plasma in which the beams interact is properly formed. All cases are conducted with the same random seeds so that the set of 18 random pseudospeckle patterns is the same from one simulation to the other.

The beam splitting parameters $N = 60$ and $\mathcal{R} = 10$ are set by comparing the near-field intensity constructed by PCGO to MIRO outputs using the OMEGA SG4 KPP data. We use a typical OMEGA 1-ns square pulse profile with 200 ps of rise time and a peak power around 25 TW, comprising a total energy of $E_{\rm tot}^{\rm SG4} = 25.7$ kJ. The total energy used in our 2D planar cases is scaled by κ in order to match the drive intensity of the 3D spherical case. The ratio κ of the average on-target intensity on the 2D cylinder $\langle I^{\rm 2D}\rangle$ to that of the average intensity on the 3D spherical capsule $\langle I^{\rm 3D}\rangle$ is

$$\kappa = \frac{\langle I^{\rm 2D}\rangle}{\langle I^{\rm 3D}\rangle} = h/2r_a, \tag{10}$$

where $h = 1$ cm and r_a is the capsule outer radius. For the capsule configuration presented in Fig. 4, $\kappa = 11.481$. The target is composed of a 66-μm-thick cryogenic DT shell and is filled with DT gas at 6.5×10^{-4} g/cm^3. Two sets of simulations are conducted with different ablators, using a 10-μm-thick plastic (CH) ablator or a 10-μm-thick cryogenic DT ablator. The Lagrangian mesh is initially cylindrical, organized with 140 cells in the radial direction and 200 in the angular direction, with a radial refinement in the ablator and shell regions. The intensity gradients imposed by the pseudospeckle patterns make necessary the use of arbitrary Lagrangian-Eulerian rezoning and remapping at each hydrodynamical time step.

B. Results and analysis

1. Absorption pattern

Figure 5 illustrates the volumic power absorbed in plasma by the inverse bremsstrahlung for cases A and B and different ablators. The absorption is naturally higher in targets with a CH ablator, owing to a higher ionization Z of the species.

We distinguish three main regions of beamlet overlap in configurations A and B (see Table I and Fig. 5). The first region covers adjacent interacting beams (for example, beams 11 and 12) and can extend from the median angle between them up to slightly beyond the edge of each beam. The second region is formed by the overlap of nearly opposed beams (for example, 2 and 11). The latter interaction regions are not visible in Fig. 5 and only occur late in the capsule implosion, when the plasma is sufficiently expanded to facilitate the intersection of beamlets from opposed beams. These regions are far from the critical density and between beamlets leaving the plasma, at similar angles with respect to the plasma flow, so there is little difference in the beams' Doppler shifts. In the geometry considered here, these intersections have negligible coupling efficiency β and have little or no influence on the laser irradiation symmetry.

In the setup presented in Fig. 5, beamlet intersections occur up to the critical density in extended regions where the plasma velocity extends from Mach 4.5 down to Mach 1 in the DT ablator case and Mach 0.5 in the CH ablator case. For a plasma flow at a velocity $\mathbf{V}$, the CBET phase-matching condition for beams of the same frequency reads

$$|\mathbf{k}_2 - \mathbf{k}_1|c_s + (\mathbf{k}_2 - \mathbf{k}_1)\cdot\mathbf{V} = 0. \tag{11}$$

Depending on the spatial configuration and propagation of the rays in plasma, there are many possible couples of Doppler-shifted $\mathbf{k}$ vectors and plasma velocities that yield non-negligible CBET gains. In general, the larger the angle is between the plasma flow and the vector $\mathbf{k}_2 - \mathbf{k}_1$, the higher the plasma flow velocity must be in order to satisfy the phase matching. This condition on the Mach number is relaxed since energy transfers between nonzero values of the frequency detuning parameter $\delta = \omega - \omega_s$ [see Eq. (8)] are taken into account. The spread in plasma flow velocities that can yield significant CBET is only limited by the spatial configurations of the beamlet $\mathbf{k}$ vectors. We identify several patterns to the energy exchanges that we refer to as the edge transfer and the core transfer (see Fig. 6). In both cases, we consider a given couple of adjacent interacting beams, i.e., separated by 20° for case A or 40° for case B.

The core transfer refers to the CBETs taking place near and in between the beams' centroids, as illustrated in Fig. 6. These exchanges occur between beamlets that are approaching the capsule at angles with the plasma flow that are slightly different. In that region, $(\mathbf{k}_2 - \mathbf{k}_1)\cdot\mathbf{V}$ is small, so the small frequency detuning can only occur for large values of the

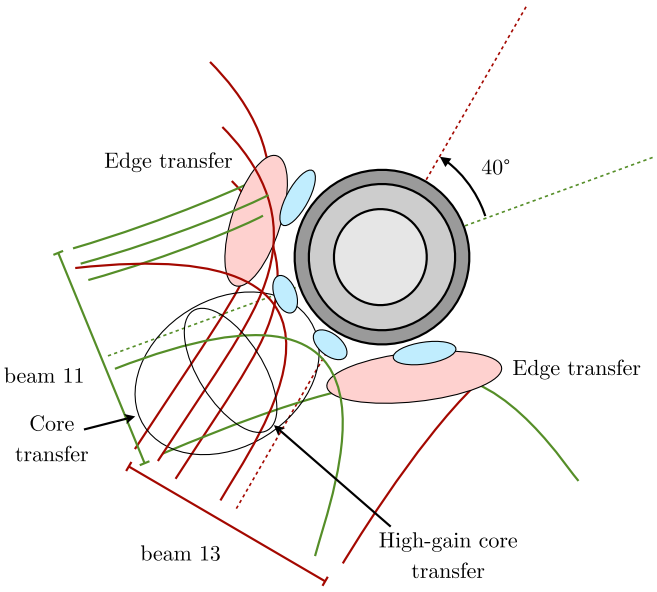

FIG. 6. (Color online) Schematic illustration of the core and edge transfers for case B. Beams 11 and 13 are shown as green (gray) and red (dark gray) lines, respectively. Increased absorption regions are shown in light red (large light gray zones) and decreased absorption regions in light blue (small light gray zones).

Mach number, i.e., away from the critical density. However, the CBET gain decreases for lower values of the plasma density and electron temperature. Consequently, there is an optimum spatial location, the so-called high-gain core region, in which the density, temperature, and Mach number are not too low for higher CBETs to occur. This region is identified by larger probe gains in Fig. 5 at about 500 and 300 μm from the critical density for cases A and B, respectively. Cross-beam energy transfer in this region is numerous and peaks at probe gains of 1.2, without a privileged direction, thus creating a noisy absorption pattern of one to two shadow regions organized around the median angle between the adjacent beams.

In the edge transfer, the left edge of the leftmost beam is intercepted by the left edge of the rightmost beam. Conversely, the right edge of the rightmost beam is intercepted by the right edge of the leftmost beam. We distinguish two types of energy exchanges: intersections between ingoing beamlets and intersections between outgoing and ingoing beamlets. The Doppler shift dictates the energy-exchange configuration. In the first case, the energy transfer occurs from the beamlet with a narrower angle to the beamlet with a broader angle (with respect to the plasma flow). In the second case, the outgoing beamlet is always amplified by the ingoing beamlet. Most power transfers observed in cases A and B completely deplete the pump beamlets. This is a consequence of the probe beamlets being amplified along their path prior to these CBETs. Most probe gain values in the edge transfer are less than 1.5 (see Fig. 5). Amplified probe beamlets create large-scale modulations in the absorption field, thus decreasing the irradiation symmetry. Moreover, interactions between outgoing and ingoing beamlets lead to a direct decrease of the coupling between the laser beam and the capsule. Laser-plasma coupling losses are a geometrical feature that are more prominent for higher convergence ratios and in the 40° cases, as is illustrated in Fig. 8. Although the net loss in total absorption induced by CBET appears moderate, edge transfer also displaces absorbed power away from the critical density, thus reducing the laser-capsule coupling further.

We note that the relatively low values of probe gains observed here, even in the edge transfer, are reasonable and adapted to the lack of a gain cutoff value. A proper implementation of a gain cutoff model is ultimately necessary, but would require significant data on dedicated CBET experiments, which is not currently available.

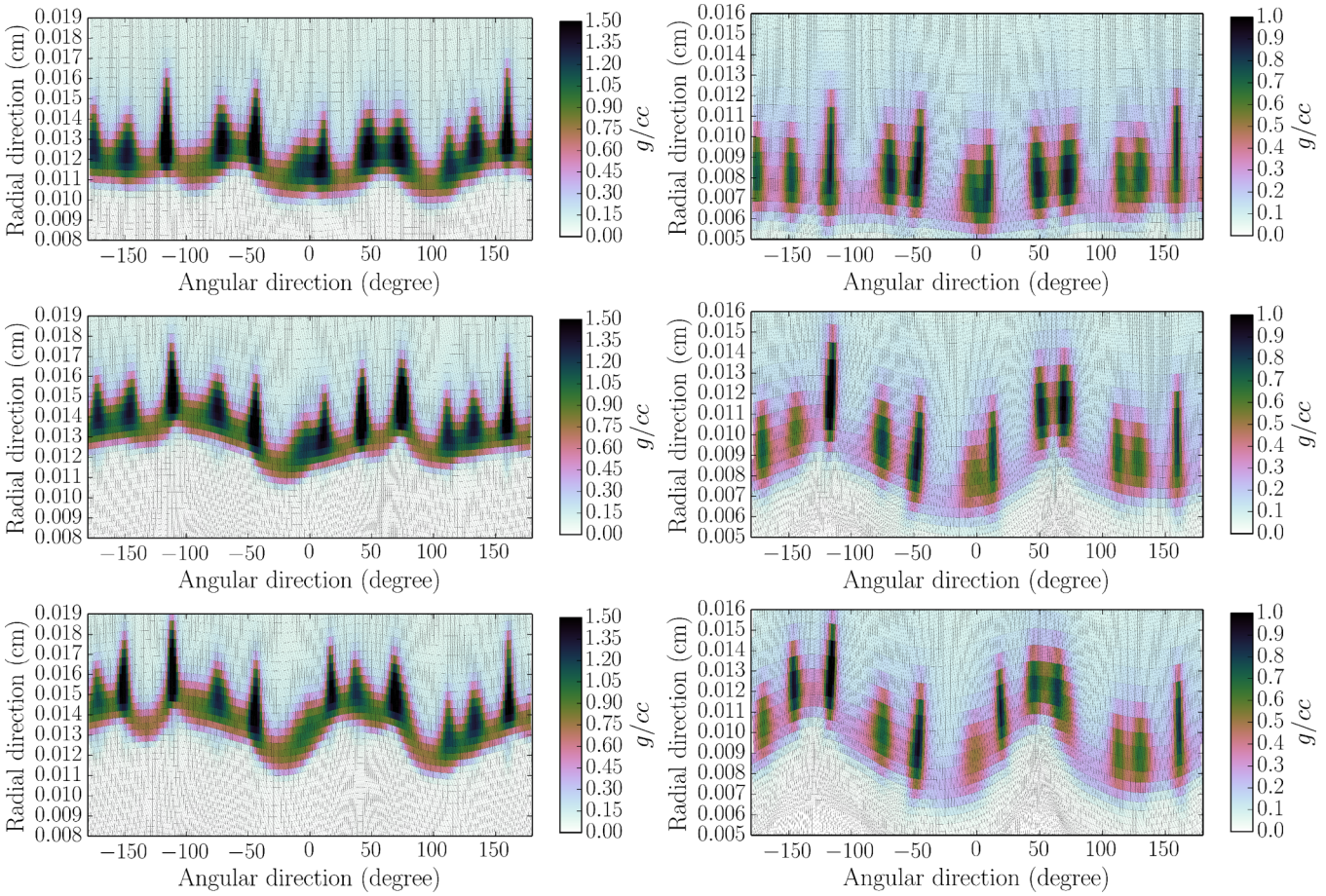

FIG. 7. (Color online) Closeup of the density field near stagnation, represented in the r-θ plane, with $\theta = 0°$ for beam 1 (see Fig. 4). The top figures are from the reference case and correspond to deformation purely arising from the pseudospeckle pattern of the lasers. The middle figures are from case A and the bottom are from case B. The figures on the left are obtained using a CH ablator and those on the right using a DT ablator. Note that for a given ablator, the y axis and color scales are the same.

TABLE II. Convergence ratios at stagnation for all cases simulated, taking the initial outer-shell radius as a reference.

Compression ratios	CH ablator	DT ablator
reference case	3.54	5.57
A	3.17	4.55
B	3.04	4.2

2. *Implosion symmetry*

The laser pulse driving the cylindrical capsule ends at $t = 1.28$ ns. Stagnation of the capsule occurs around $t = 1.31$ ns for the CH ablator case and around $t = 1.33$ ns for the DT ablator. At that point, modulations in the capsule density profile constitute a time- and space-integrated proxy of the laser illumination modulations arising from the pseudospeckle pattern and CBET. Simulations are analyzed at stagnation, i.e., around $t = 1.31$ ns.

Figure 7 shows the shell density profile in the r-θ plane for the reference case (top), case A (middle), and case B (bottom). The DT ablator targets (right) achieve higher convergence ratios than the CH ablator ones (left), a direct consequence of them being lighter and subject to the same laser intensity. Two-dimensional convergence ratios computed from the target's initial radius of the outer shell, i.e., $r_s = 425$ μm, are shown in Table II. Cross-beam energy transfer decreases the convergence ratio with respect to the reference case, by up to 14% for the CH ablator target and 25% for the DT ablator target. As demonstrated in Sec. IV B 1, the edge transfers between outgoing and ingoing portions of the beams take energy away from the capsule, thus decreasing the laser-capsule coupling efficiency and consequently the convergence ratio. This is consistent with the decrease in integrated absorption noted in Fig. 8.

In order to conduct a Fourier decomposition of the shell modes, we identify the internal (external) interfaces at a given θ as the positive (negative) maximum of the derivative of the density in the r direction. Assuming that at least 6 points in θ are needed in order to correctly describe a Fourier mode, the higher mode that can be characterized in our simulations with 200 angular points is mode 33. Internal and external interface profiles are smoothed using a Hann window of 6 points in length and fitted using least squares to Fourier modes up to order 33. The resulting internal interface mode amplitudes with respect to the reference are shown in Fig. 9 (mode 0 is not shown).

The CH ablator target in the reference case (Fig. 7, top left) presents small-scale modulations on the external interface, corresponding to lumps of high-density regions resembling fingers. Because the simulations are 2D planar and the convergence ratios rather low, the high amplitude of the deformations and the lumps of matter do not lead to the shell breakdown. High-frequency modulations are smoothed out when reaching the internal interface, greatly reducing the power density of Fourier modes higher than 5. Significant long-wavelength deformations are present at the internal interface, corresponding to modes 1, 3, and 4. The highest deformation present in the internal interface is of about 10% relative amplitude, measured as a half peak-to-peak amplitude

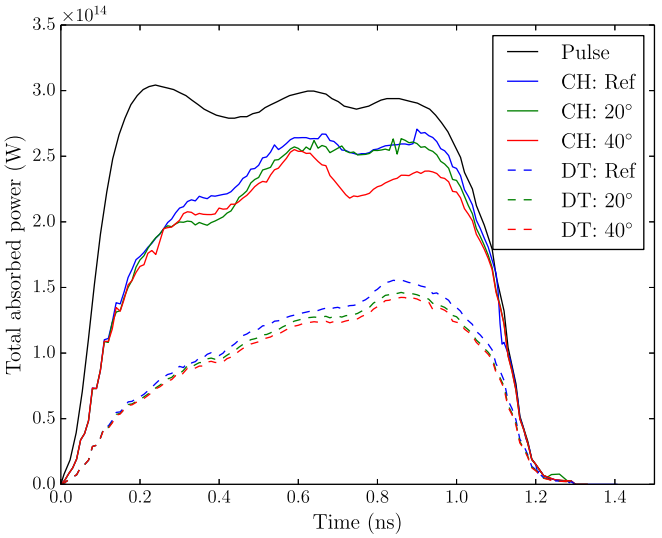

FIG. 8. (Color online) Power absorbed by the plasma by inverse bremsstrahlung as a function of time shown as blue (gray) lines for the reference case, green (light gray) lines for case A, and red (lighter gray) lines for case B. Results are shown as solid lines for CH ablator simulations and dashed lines for DT ablator simulations. The drive pulse is shown as a black solid line. The 2D power is scaled by κ (see Sec. IV A).

(see Fig. 10, top). These modulations can be seen as the imprint of the beam configuration, including the effect of the pseudospeckle pattern. In order to dissociate the effects of CBET to that of the pseudospeckle pattern, the Fourier modes are compared to the reference case.

The Fourier analysis of the internal interface shows that CBET amplifies low modes 2 and 8 (the CH ablator case). This can be seen in Fig. 10 (top) as an oblate deformation of the inner interface of the shell, reaching a relative amplitude of about 13.5% for case A and 15% for case B. The dominant presence of mode 2 is a consequence of the higher-absorption regions from the amplified edges of the beams, regions that are nearly symmetrical with respect to those of the opposed beams. Although these could also lead to mode 4 deformations, the use of noninteracting beams to provide the cylindrical ablation pressure effectively smoothes those modes (e.g., beams 6, 7, 16, and 17), which would not be the case in a 3D configuration.

The DT ablator targets (Fig. 7, right) also feature patterns of lumps of density arranged in fingers, but to a point where there is almost no more shell mass between those and the capsule can be considered as punctured or broken. Cases A and B show a significant shell deformation of low modes 2 and 8. Since this case is more sensitive to energy exchanges due to a lower Z of the plasma, the effects of CBET are exacerbated and mode 2 is very prominent. The inner interface of the target reaches a maximum deformation of a relative amplitude of 24% in the reference case, 34% in case A, and 31% in case B. Modes 6 and 8 present in DT and CH ablator cases are created by the six or eight shadow regions from the edge and core transfer, this number depending on the CBET geometries created by the core transfer.

The OMEGA chamber beam port configuration can be decomposed in eight adjacent constant azimuth planes, between

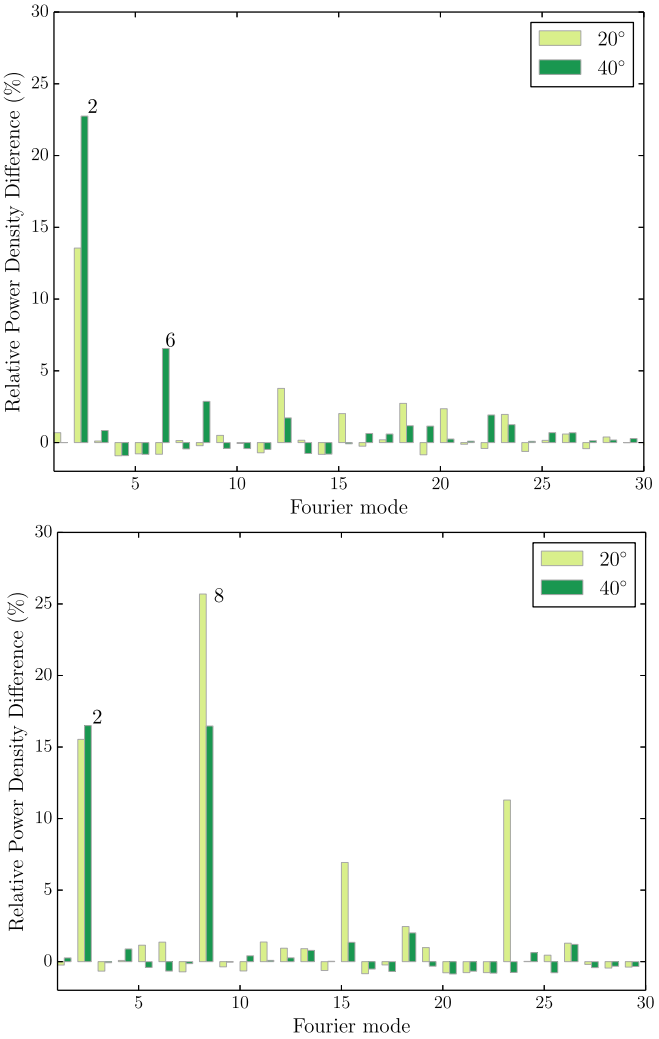

FIG. 9. (Color online) Relative power density histograms of the inner-shell interface Fourier modes, for the CH ablator case (top) and the DT ablator case (bottom), near stagnation. Relative power densities $\hat{p}$ are computed as $\hat{p} = (p_{\text{ref}} - p)/p_{\text{ref}}$, where p_{ref} and p are mode power densities of the reference case and the corresponding case, respectively. Case A is shown in light green (light gray) and case B in dark green (dark gray). Mode 0 is not shown.

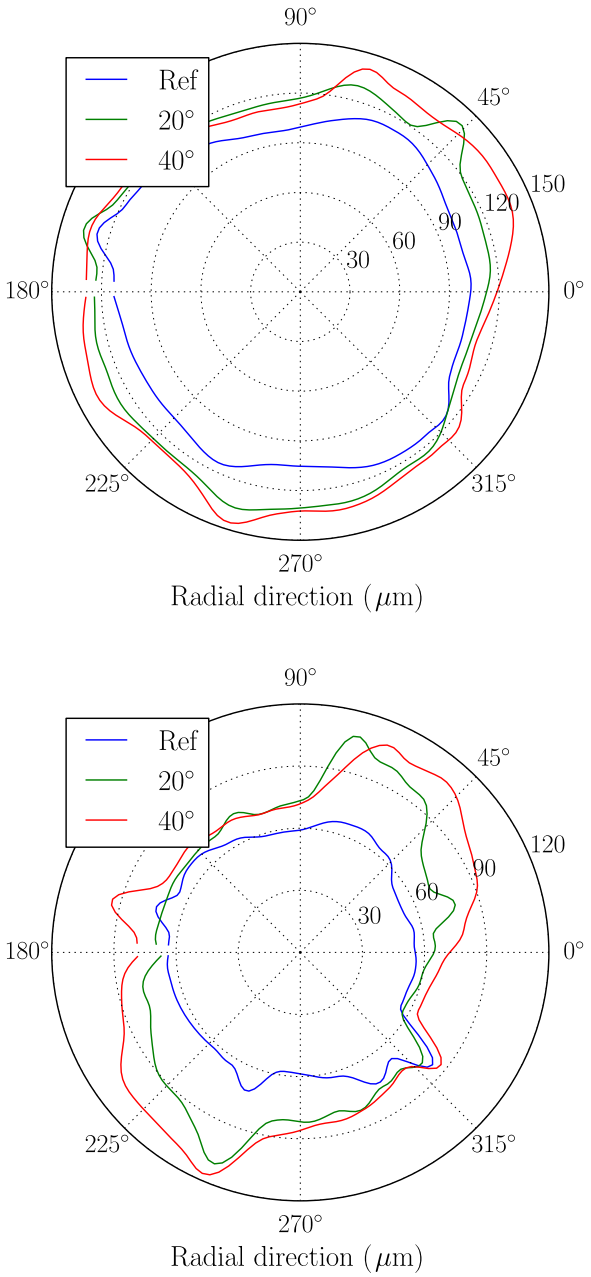

FIG. 10. (Color online) Internal interface of the capsule near stagnation for the CH ablator case (top) and the DT ablator case (bottom). Reference simulations are shown as blue lines (gray), case A simulations as green lines (light gray), and case B simulations as red lines (lighter gray).

which the coplanar interacting beams' median angle is offset by an elevation of 20°−80° depending on the azimuthal angle. It is thus expected that the mode 2 deformation imposed by CBET in the planar configuration creates higher-order modes in a full 3D configuration. This can be estimated by making a linear combination of planar simulation results so as to reproduce the 3D OMEGA sphere configuration. Simulation results for the internal shell interface at stagnation are combined using one set of results per discrete azimuthal increment (see the OMEGA beam configuration in Appendix C), which corresponds to either the 20° or 40° CBET case, shifted by the corresponding elevation angle value. The combined data set reproduces a spherical capsule from a linear combination of 2D planar simulations. We decompose this shell in the spherical harmonics Y_l^m up to $l = 14$ for all values of m. This is done using the simulation results with and without CBET.

The difference in mode amplitudes is shown in Fig. 11, along with the combined data set for the CBET case and its spherical harmonics fit. This linear analysis shows that CBET amplifies the spherical mode $l = 2$ similarly to the planar case because of a combination of Y_2^{-2} and Y_2^0. Although even and odd modes are equally present in the intensity distribution on the capsule, only even modes are amplified by CBET, while the odd modes remain unchanged. Mode $l = 4$, which was not excited by CBET in the 2D simulations, contributes more significantly to the overall 3D shell deformation, mainly through Y_4^3. We retrieve excitation of modes $l = 6$ and 8, as well as

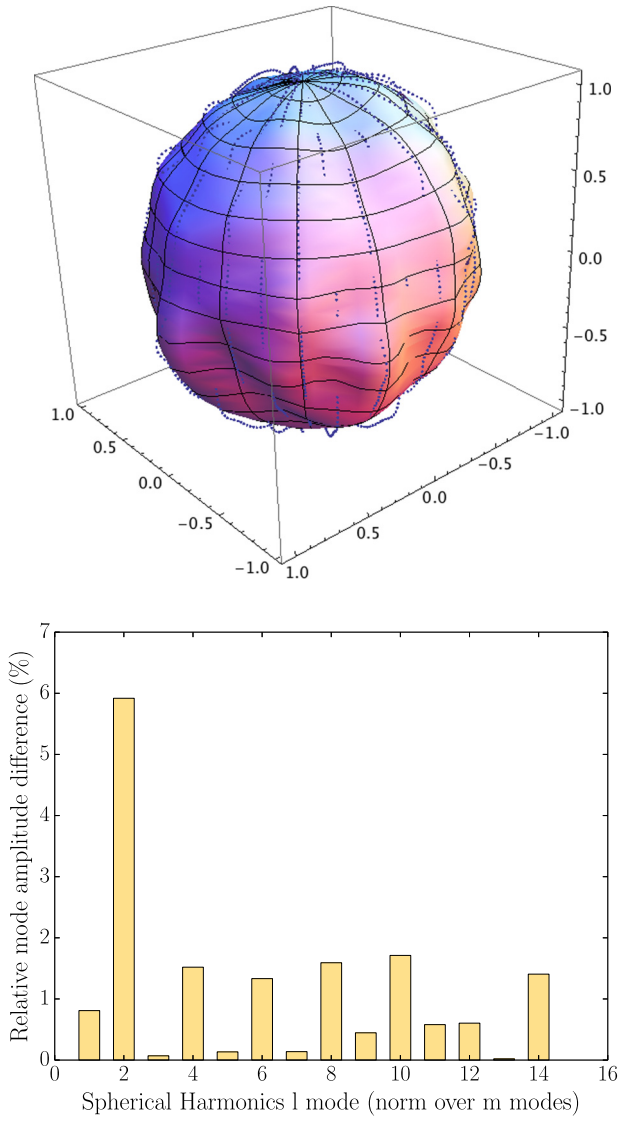

FIG. 11. (Color online) Shown on the top is the 3D internal shell surface perturbation near stagnation for the CBET case, constructed as a linear combination of several 2D planar simulations. Simulation results are shown as blue (light gray) dots and the corresponding spherical harmonics fit is superimposed as a colored (grayscale) surface. The bottom shows the relative mode amplitude difference $\hat{a}_l = |a_l^{\text{ref}} - a_l|/a_l^{\text{ref}}$, where a_l^{ref} and a_l are l-mode amplitudes for the reference case and the CBET case, respectively. The a_l modes are computed by taking the L_2 norm over the corresponding m modes. Mode 0 is not represented.

higher-order even modes. Although this linear combination of results does not include any interaction between azimuthal planes, it provides a rough estimate of potentially excited modes by CBET, arising only from the beam port configuration.

V. CONCLUSION

We presented a method to model realistic ICF beams using paraxial complex geometrical optics in the framework of a large-scale radiative hydrocode. Beam splitting in small beamlets and pseudorandom focusing was used in order to reproduce the main features of the intensity field of a large beam transformed by a KPP. Comparisons were conducted with the laser propagation code MIRO in the case of the OMEGA SG4 beam configuration. The splitting algorithm produces a pattern of large speckles (or pseudospeckles) that exhibits intensity distributions and laser contrast similar to the results from MIRO convolved with the hydrodynamical mesh resolution.

Paraxial complex geometrical optics allows access to key quantities in the plasma, such as the beamlet intensity profile, curvature radius, and width. Cross-beam energy transfer based on PCGO is implemented in the hydrocode CHIC. The CBET model takes into account energy exchanges between pairs of beamlets and consistently resolves power transfers. The pairwise CBET interactions were resolved chronologically by coupling consequent energy exchanges with updates of the downstream beamlet parameters through reintegration of the Riccati equations along the beamlets trajectories. Power transfers were computed in the steady-state approximation and interacting beams were supposed to preserve a Gaussian shape with a constant width across the pointlike interaction region.

We applied both PCGO-based models of realistic beam modeling and CBET to the OMEGA beam configuration with the SG4 KPP in a 2D planar geometry. We conducted full 360° simulations of a capsule implosion in which certain beams were allowed to interact through CBET, following the relevant coplanar beam angles of 20°, 40°, 140°, and 160°. The influence of the ablator material was assessed by repeating these simulations in the CH and DT ablator cases. The influence of modeling a pseudospeckle pattern on the power deposition field and capsule implosion symmetry was studied as a reference case for comparisons with simulations with the same pseudospeckle patterns but with CBET enabled. In the reference case without CBET, the power deposition profile exhibits a pseudospeckle pattern that is relatively smoothed out by the overlap of the beams. The internal shell interface is deformed by low-amplitude long-wavelength Fourier modes 1–4. A variety of high-frequency modes up to mode 33 were observed and greatly smoothed out when reaching the internal shell interface. Simulations with main CBET angles at 20° and 40° show that in those configurations CBET tends to create a pattern of high- and low-absorption regions through specific regimes of core and edge power transfers, significantly amplifying modes 2, 6, and 8 of the internal shell interface. A reconstruction of the shell based on a linear combination of planar results suggests that mode 4 is also likely to be excited by CBET in a full 3D configuration. The choice of the ablator material is seen to be critical in terms of CBET, with lower-Z materials presenting more efficient energy exchanges and thus higher-shell deformations. We observe relative deformations of the inner-shell interface at stagnation of up to 15% in the CH ablator case and 34% in the DT ablator case. Cross-beam energy transfer is also seen to have an effect on the global laser-plasma coupling, by reducing the total amount of energy transferred to the plasma. two-dimensional convergence ratios are lower when enabling CBET by up to 14% for the CH ablator case and 25% for the DT ablator case.

Such results highlight the importance of modeling nonlinear LPI in large-scale hydrocodes for the design of direct-drive ICF

targets and laser configurations. In particular, shock ignition involves high laser intensities at the late stages of the capsule implosion, the time at which the beam configuration may lead to numerous CBETs and reduce the efficiency of the ignition method.

ACKNOWLEDGMENTS

The authors wish to thank the anonymous reviewers for very interesting discussions and constructive comments. We also wish to thank Ph. Nicolaï and J. Breil for their help. This work was partially supported by the EURATOM within "Keep in Touch" activities and Project No. ANR-12-BS04-0006-04 from the French National Agency of Research.

APPENDIX A: SUPER-GAUSSIAN SPLITTING

The intensity distribution computed at the virtual circle I_v^{FFT} (see Sec. II B) is approximated by a super-Gaussian intensity distribution I_v through a nonlinear least-squares fit. The latter intensity distribution reads

$$I_v = I_{0v} \exp\left(-\left|\frac{y}{r_v}\right|^{n_v}\right). \tag{A1}$$

We assume that the Gaussian distributions (beamlets) have identical widths $\hat{r_v}$ and are equally spaced in the $[-r_v,r_v]$ interval. The splitting problem then reads

$$I_v = \sum_{k=1}^{N} I_{0v}^k \exp\left[-2\left(\frac{y - r_v[2(k-1)/(N-1)-1]}{w_v^k}\right)^2\right]. \tag{A2}$$

We define an analytical expression for I_{0v}^k,

$$I_{0v}^k = \frac{3\hat{\mathcal{R}} I_{0v}}{N-1}\mathcal{C}_{\hat{\mathcal{R}}} \exp\left(-2\left|2\frac{k-1}{N-1}-1\right|^{n_v}\right),$$
$$\mathcal{C}_{\hat{\mathcal{R}}} = 0.532\,19 - \frac{3.801\,67\times10^{-3}}{\hat{\mathcal{R}}} + \frac{1.8226\times10^{-1}}{\hat{\mathcal{R}}^2}, \tag{A3}$$

where $\hat{\mathcal{R}}$ is the ratio of the beamlet radius at a virtual circle to the beam radius at a virtual circle. Here $\hat{\mathcal{R}}$ is computed from $\mathcal{R}$ using the beamlet's Rayleigh range. The coefficients in $\mathcal{C}_{\hat{\mathcal{R}}}$ were obtained numerically by a least-squares fit. Defining I_v^{div} as the intensity obtained by summing the beamlet intensity profiles at the splitting coordinates, we write the mean-square error (MSE) of the decomposition as

$$\mathrm{MSE} = \frac{1}{10r_v}\int_{-5r_v}^{5r_v}\left[I_v^{\mathrm{div}}(r) - I_v(r)\right]^2 dr. \tag{A4}$$

The MSE is found to decrease with increasing $\hat{\mathcal{R}}$, with small values from $\hat{\mathcal{R}} = 3$. The error is small and rather independent of n_v for values higher than 5, with the minimum being below 5. The number of beamlets used to compute the error is $N = 3\hat{\mathcal{R}}$ and constitutes an indication of the minimum of beamlets to use. In practice, one will use many more beamlets in order to obtain a correct beam contrast in the near field ($\sim 5N$ minimum; see Sec. II C). The value of $\hat{\mathcal{R}}$ that can be chosen has an upper limit determined by the size of the pseudospeckles at the focal plane, which must be larger than a few wavelengths in order to satisfy the validity domain of PCGO.

APPENDIX B: CROSS-BEAM ENERGY-TRANSFER IMPLEMENTATION

1. Intersection identification

We simplify the problem of thick-ray CBET by considering only intersections between beamlets whose central rays cross. By doing so, we neglect partial power transfers between beamlet envelopes. This approach is reasonable in a 2D configuration because the thick rays' centroids intersect often. However, it would not be viable in a 3D code. The central ray trajectories in the plasma are computed using the RT model, which PCGO is based on [12,13]. In a typical direct-drive ICF configuration, the mesh refinement in the ablator or capsule outer shell is very high and cells are very thin. The intersection found in that region is prone to numerical errors if there is a lack of precision in the ray trajectories. Ray-tracing models are often based on fourth-order Runge-Kutta algorithms, whose accuracy greatly falls off in regions of thin cells and a low optical index. This problem has been treated by modifying the RT model in our hydrodynamic code CHIC to include adaptive error control and step corrections using analytical solutions for ray trajectories in triangles of a constant density gradient. In order to find an intersection between rays, we identify cells in which at least two rays are propagating. In a given triangle, the (x,y) coordinates of central rays 1 and 2 are given by the parametric equations [13]

$$\begin{aligned} x_1(t) &= a_{x1}t^2 + v_{x01}t + x_{01},\\ y_1(t) &= a_{y1}t^2 + v_{y01}t + y_{01},\\ x_2(s) &= a_{x2}s^2 + v_{x02}s + x_{02},\\ y_2(s) &= a_{y2}s^2 + v_{y02}s + y_{02}, \end{aligned} \tag{B1}$$

where $s \in [0,s_f]$ and $t \in [0,t_f]$ with s_f and t_f the rays' parametric coordinates at the exit of the triangle. For two beamlets with the same frequency, $a_{x1} = a_{x2}$ and $a_{y1} = a_{y2}$. We assume that the frequency difference between two beamlets is small enough in general so that we can define $a_x = (a_{x1} + a_{x2})/2$ and $a_y = (a_{y1} + a_{y2})/2$. In the particular cases presented in this paper, all beams have the same frequency and CBET is only induced by the Doppler shift, which does not affect beam trajectories. The intersection between the two rays can be found by solving Eq. (B1) for s_i and t_i such as

$$\begin{aligned} a_x t_i^2 + v_{x01}t_i + x_{01} &= a_x s_i^2 + v_{x02}s_i + x_{02},\\ a_y t_i^2 + v_{y01}t_i + y_{01} &= a_y s_i^2 + v_{y02}s_i + y_{02}, \end{aligned} \tag{B2}$$

$$s_i \in [0,s_f], \quad t_i \in [0,t_f] \tag{B3}$$

Two sets of analytical solutions (s_{i1},t_{i2}) and (s_{i2},t_{i2}) can be found for Eqs. (B2). These solutions may be out of the interval (B3) so that rays may not intersect. These solutions should be computed in extended quadruple precision in order to limit numerical errors, erroneous intersection coordinates, and false duplicates.

Once a set (s_i,t_i) has been found, the intersection coordinates (x_c,y_c) can be computed. These coordinates are used for

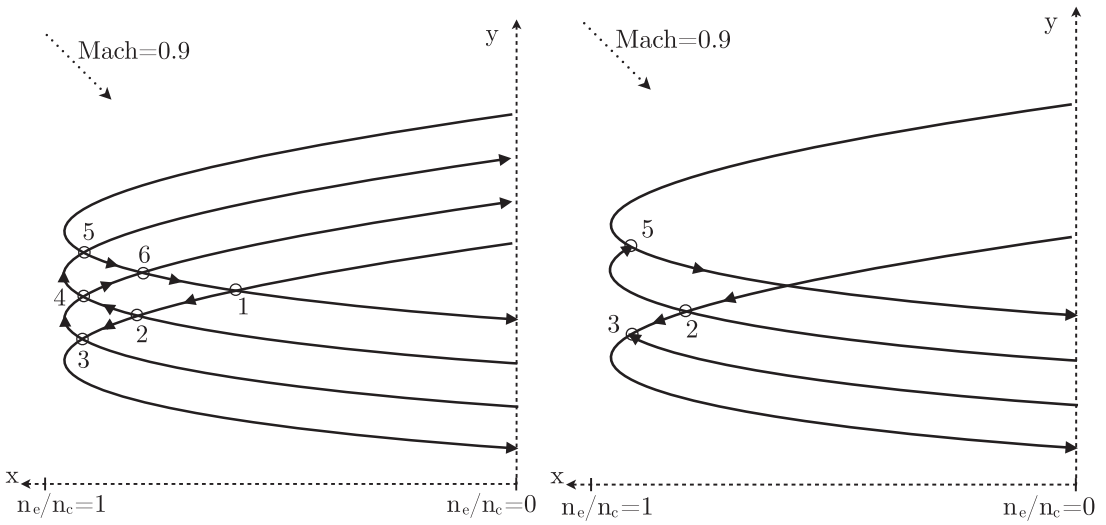

FIG. 12. Beamlets incident on a linear density ramp from $n_e/n_c = 0$ to $n_e/n_c = 1$ with an angle of 10°. All beamlets have the same wavelength and a Mach $M = 0.9$ flow is imposed at 45°. The six intersections on the left have a significant and non-negligible coupling coefficient β. One can identify one 4-loop {1,2,4,6}, two 5-loops {1,2,3,4,6} and {1,2,4,5,6}, and one 6-loop {1,2,3,4,5,6}. The loops are analyzed in increasing degrees of complexity and the lower β node is removed. The CBET in the simplified diagram on the right can now be computed by solving node 2 first and nodes 3 and 5 in any order. In that configuration, rays with upshifted frequencies in nodes 3 and 5 lose all their energy in the CBET.

the interpolation of plasma quantities in the computation of Doppler frequency shift, plasma parameters, and CBET gain.

2. Intersection ordering

At each hydrodynamical time step, the intersections between central rays of the PCGO model are identified. The resulting set of intersections is potentially large and usually reaches up to 10 000 intersections in direct-drive target configurations. For the CBET model to be consistent, these energy transfers must be resolved in chronological order with respect to each ray's propagation. For an energy transfer to be computed at a given intersection, the two rays involved must not be involved in a previous intersection, or only in previous intersections where energy transfer has already been taken into account. Once an intersection has been computed, the beamlets' energies are updated (through their intensity) and are propagated once again from the intersection to the next one by solving the Riccati equations [13] in the plasma.

Considering CBET between two rays at a time, a given intersection i depends on at most two direct downstream intersections (children) and two direct upstream intersections (parents). The ordering of the intersections (nodes) starts by finding the nodes that have no parents. We define those as being level 0. We consider a node to be ordered if all of its parents are ordered. By definition, level 0 nodes are ordered. During the solution process, we keep track of nodes for which one of two parents is ordered. Those nodes are referred to as the temporary set.

From a given level i of nodes (starting from 0), we form a set from the union of the children of level i nodes and the temporary set. Across the nodes of this newly constructed set, we look for ordered nodes to construct the level $i + 1$. Nodes in $i + 1$ that were in the temporary set are removed. Children of nodes in i that have not been resolved are added to the temporary set. The operation is then repeated from level $i + 1$ until the whole intersection tree has been ordered.

3. Finding and resolving loops in the intersection tree

Before applying the above algorithm to a set of nodes, one must ensure that the set can be ordered. In particular, loops in the intersection topology must be simplified for intersections to be treated in a logical order. Identifying loops is simple in principle but can be computationally challenging depending on the size of the loops and the total number of intersections. We define an intersection i as being in a loop of order n if i is in the nth generations of its own children (see Fig. 12 for an example).

Loops are identified in ascending loop length order from 2 to 20. For each loop identified, the intersection for which the CBET coupling coefficient is the lowest is removed. The intersection tree is simplified before further loop finding is applied by computing the energy exchange between the beamlets and eventually eliminating intersections containing at least one depleted beamlet.

APPENDIX C: ANGULAR CONFIGURATION OF OMEGA BEAMS

Since the PCGO model implemented in the hydrocode CHIC is two dimensional [13], we look for configurations where beams are coplanar in a plane passing by the capsule center. The latter planes can be visualized in an azimuthal-elevation diagram, where these angles are defined on the left-hand side of Fig. 13. The right-hand side of Fig. 13 illustrates the beam positions with respect to their azimuthal angle and elevation angle. At a given azimuthal angle, beams are coplanar and the corresponding plane passes through the capsule center. These planes can be used as a 2D simulation configuration for the PCGO model.

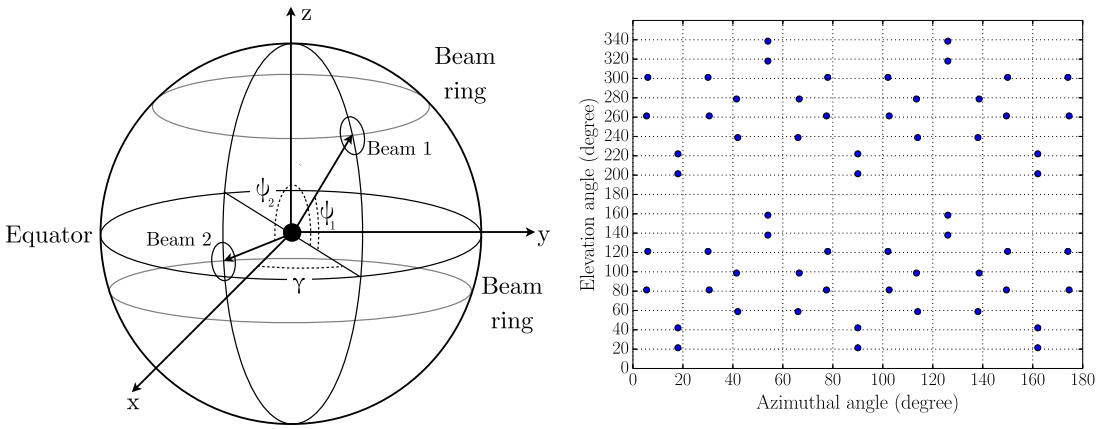

FIG. 13. (Color online) Shown on the left is the definition of the azimuthal angle γ and elevation angle ψ. The entire sphere can be characterized with $\gamma \in [0,180]^\circ$ and $\psi \in [0,360]^\circ$. In this example, beams 1 and 2 are on the same azimuthal plane and at different elevation angles ψ_1 and ψ_2. The configuration on the right is of the 60 OMEGA beam ports in azimuthal-elevation angular coordinates. At a fixed γ, adjacent beams are separated by 20° or 40°. By considering adjacent γ planes, we could consider 2D interactions between beams with higher angular separations.

[1] J. Nuckolls, L. Wood, A. Thiessen, and G. Zimmerman, Nature (London) **239**, 139 (1972).

[2] J. Lindl, Phys. Plasmas **2**, 3933 (1995).

[3] S. Atzeni and J. Meyer-ter Vehn, *The Physics of Inertial Fusion*, International Series of Monographs on Physics (Oxford University Press, Oxford, 2004).

[4] L. Divol, R. L. Berger, N. B. Meezan, D. H. Froula, S. Dixit, L. J. Suter, and S. H. Glenzer, Phys. Rev. Lett. **100**, 255001 (2008).

[5] D. H. Froula, L. Divol, R. A. London, R. L. Berger, T. Döppner, N. B. Meezan, J. S. Ross, L. J. Suter, C. Sorce, and S. H. Glenzer, Phys. Rev. Lett. **103**, 045006 (2009).

[6] P. Michel, L. Divol, E. A. Williams, S. Weber, C. A. Thomas, D. A. Callahan, S. W. Haan, J. D. Salmonson, S. Dixit, D. E. Hinkel, M. J. Edwards, B. J. MacGowan, J. D. Lindl, S. H. Glenzer, and L. J. Suter, Phys. Rev. Lett. **102**, 025004 (2009).

[7] I. V. Igumenshchev, D. H. Edgell, V. N. Goncharov, J. A. Delettrez, A. V. Maximov, J. F. Myatt, W. Seka, A. Shvydky, S. Skupsky, and C. Stoeckl, Phys. Plasmas **17**, 122708 (2010).

[8] I. V. Igumenshchev *et al.*, Phys. Plasmas **19**, 056314 (2012).

[9] V. N. Goncharov *et al.*, Phys. Plasmas **21**, 056315 (2014).

[10] J. F. Myatt, J. Zhang, R. W. Short, A. V. Maximov, W. Seka, D. H. Froula, D. H. Edgell, D. T. Michel, I. V. Igumenshchev, D. E. Hinkel, P. Michel, and J. D. Moody, Phys. Plasmas **21**, 055501 (2014).

[11] D. Batani, S. Baton, A. Casner, S. Depierreux, M. Hohenberger, O. Klimo, M. Koenig, C. Labaune, X. Ribeyre, C. Rousseaux, G. Schurtz, W. Theobald, and V. T. Tikhonchuk, Nucl. Fusion **54**, 054009 (2014).

[12] T. B. Kaiser, Phys. Rev. E **61**, 895 (2000).

[13] A. Colaïtis, G. Duchateau, P. Nicolaï, and V. Tikhonchuk, Phys. Rev. E **89**, 033101 (2014).

[14] P. Michel *et al.*, Phys. Plasmas **17**, 056305 (2010).

[15] Yu. A. Kravtsov, Radiophys. Quantum Electron. **10**, 719 (1967).

[16] Y. A. Kravtsov and P. Berczynski, Stud. Geophys. Geod. **51**, 1 (2007).

[17] T. R. Boehly, D. L. Brown, R. S. Craxton, R. L. Keck, J. P. Knauer, J. H. Kelly, T. J. Kessler, S. A. Kumpan, S. J. Loucks, S. A. Letzring, F. J. Marshall, R. L. McCrory, S. F. B. Morse, W. Seka, J. M. Soures, and C. P. Verdon, Opt. Commun. **133**, 495 (1997).

[18] O. Morice, Opt. Eng. **42**, 1530 (2003).

[19] O. Morice, X. Ribeyre, and V. Rivoire, in *Third International Conference on Solid State Lasers for Application to Inertial Confinement*, edited by W. H. Lowdermilk, Proceedings of SPIE Vol. 3492 (SPIE, Bellingham, 1999), pp. 832–838.

[20] Ph. Donnat, CEA report, 1998 (unpublished).

[21] J. Garnier, C. Gouédard, and L. Videau, Opt. Commun. **176**, 281 (2000).

[22] R. L. McCrory *et al.*, Eur. Phys. J. D **44**, 233 (2007).

[23] C. J. McKinstrie, A. V. Kanaev, V. T. Tikhonchuk, R. E. Giacone, and H. X. Vu, Phys. Plasmas **5**, 1142 (1998).

[24] C. J. McKinstrie, J. S. Li, R. E. Giacone, and H. X. Vu, Phys. Plasmas **3**, 2686 (1996).

[25] P. Loiseau, Ph.D. thesis, Université Bordeaux 1, 1999.